https://doi.org/10.1007/s41230-026-5052-2

Tolerance-constrained inverse design of ceramic core configuration for precision wall thickness control in hollow turbine blades

Zi-chun Wang[1, 2, 3], Wen-hu Wang[1, 2, 3], *Kang Cui[4], Rui-song Jiang[5], Rui-zhe Dong[1, 2, 3], and Yuan-bin Wang[1, 2, 3]

1. *Key Laboratory of High-Performance Manufacturing for Aero Engine, Ministry of Industry and Information Technology, School of Mechanical Engineering, Northwestern Polytechnical University, Xi'an 710072, China*
2. *Engineering Research Center of Advanced Manufacturing Technology for Aero Engine, Ministry of Education, School of Mechanical Engineering, Northwestern Polytechnical University, Xi'an 710072, China*
3. *State Key Laboratory of Cemented Carbide, School of Mechanical Engineering, Northwestern Polytechnical University, Xi'an 710072, China*
4. *School of Automation and Software Engineering, Shanxi University, Taiyuan 030006, China*
5. *School of Mechanical Engineering, Sichuan University, Chengdu 610065, China*

Abstract: Wall thickness deviation significantly diminishes the durability and efficiency of turbine blades. It primarily results from surface deformation and positional shifts of the ceramic core during casting, which disrupts core-shell alignment. A novel reverse adjustment method for ceramic core positions within turbine blades based on the measurement of a batch of blades was proposed in this work. Initially, the optimal position solution model for internal ceramic cores of turbine blades on the basis of industrial computed tomography (ICT) scanning was established. Subsequently, a reverse adjustment method was developed to optimize the position and orientation of ceramic cores within the blade interior. The proposed method was verified through casting experiments, revealing a reduction of 45.5% in the maximum wall thickness error of the adjusted blades compared to their initial condition. The wall thickness error at the leading and trailing edges of the blade is reduced to less than ±0.15 mm, while the wall thickness error on the concave and convex surfaces is minimized to less than ±0.2 mm, which essentially satisfies the prescribed wall thickness tolerance requirements. The process system for precise shape control of hollow turbine blade wall thickness is further refined, providing robust technical support for enhancing the conformity rate of hollow turbine blade wall thickness dimensions.

Keywords: hollow turbine blade; tolerance-constrained; wall thickness control; reverse adjustment; model alignment

CLC numbers: TG249.5 **Document code:** A **Article ID:** 1672-6421(2026)04-599-14

1 Introduction

Turbine blades, which are an essential component of aeroengines, possess complex hollow structures with internal cooling systems, are primarily made of superalloy. This design is crucial for meeting rigorous performance demands in high-temperature and high-pressure conditions[1, 2]. In turbine blade manufacturing, the suitable wall thickness is vital to ensure enough strength, cooling effectiveness, and service life. Thinner walls weaken the structure and lead to potential fractures, whereas thicker walls may impede cooling efficiency, elevating the risk of overheating and blade damage[3, 4]. Currently, attaining precise control of the wall thickness in hollow turbine blades faces a significant technical challenge in aero-engine manufacturing.

Hollow turbine blades are predominantly manufactured by investment casting. The process includes several steps, such as ceramic core preparation, wax injection, shelling, dewaxing, pouring, and other machining processes[5, 6]. The success of the casting process is influenced by factors such as the thickness of the wax pattern and the alignment between the ceramic core and the shell mold[7-9].

***Kang Cui**

Male, born in 1985, Ph. D., Associate Professor. His research interests include investment casting technology, additive manufacturing, and intelligent manufacturing.

E-mail: cuikang@sxu.edu.cn
Received: 2025-03-07; Revised: 2025-06-25; Accepted: 2025-12-01

In recent years, significant research efforts have been dedicated to controlling turbine blade profiles and wall thickness, with a focus on tracing and analyzing these parameters throughout the investment casting process. In addressing the issue of ceramic core surface deformation, research has focused primarily on improving the structural strength of the ceramic core at high temperatures by controlling the compositions of the ceramic core[10-12]. In the preparation of the wax pattern, numerical simulation was employed to analyze the wax injection process and the flow behavior of wax materials under different temperature conditions[13-15]. To optimize the process parameters for wax injection, the influence of process parameters on the internal pressure distribution within the die cavity and the dimensional shrinkage of the wax pattern was investigated[16-18]. On this basis, the wax injection process and the metal pouring process were analyzed as an integrated system. By examining the dimensional shrinkage behavior of the deformed wax pattern, the shrinkage allowance of the casting can be accurately controlled, thereby ensuring precise regulation of the profile and wall thickness dimensions of the turbine blade casting[19]. To adjust the position of the ceramic core within the wax pattern die, a novel approach of integrating rigid body kinematics with heuristic algorithms was proposed[20]. This approach established an effective strategy to adjust the orientation of the ceramic core, enabling precise control over the wall thickness of the wax pattern[21, 22]. In addition, an optimization method for wax pattern die cavities based on the anti-deformation principle was proposed. By addressing the volume shrinkage issues of various materials during the casting process and applying the anti-deformation principle to refine the profile of the wax pattern die cavity, this method enabled precise control over the dimensions of the blade's external surface[23]. In the shelling, Dong et al.[24] optimized the shell thickness uniformity of the shell mold by adjusting the attitude angle and module diameter, thereby enhancing the structural integrity and dimensional accuracy of the blade. Zhao et al.[25] used finite element simulation to analyze the influence of shell roasting temperature on the dimensional accuracy of blade castings. The flow field, temperature field, and shrinkage porosity of vacuum precision casting were simulated using ProCAST software, and the optimal shell preheating temperature and pouring temperature were obtained[26]. In the subsequent casting process, scholars primarily addressed the issue of blade cross-section deformation resulting from casting process parameters and solidification, effectively mitigating deviations in blade appearance dimensions to ensure stable control of the casting process[27-29].

The aforementioned methods primarily focus on maintaining process stability at each stage of the investment casting process to ensure dimensional accuracy of the hollow turbine blade, as shown in Fig. 1. Despite its effectiveness, limitations have been highlighted by deviation analysis during batch production, particularly issues arising from the partial free-end position of the ceramic core within the shell. The impact of the molten metal during pouring causes the ceramic core to shift, while fabrication errors in the manufacturing process affect its alignment with the shell. These issues lead to significant deviations in the blade's wall thickness. Therefore, this study analyzes ceramic core positions after casting in actual batches, considering the potential impact of core shift on blade wall thickness during casting. The objective is to establish a reverse control method for adjusting ceramic core position within the blades by studying core shift from the initial position to the final casting blades.

In fact, the problem of adjusting the position of ceramic cores inside the wax pattern die cavity can be divided into two parts: The first is the matching problem between the ceramic core and shell, which is essentially the domain of model registration, assuming that the shifting position of ceramic cores during casting is considered as a rigid-body motion transformation. The classic ICP (Iterative Closest Point) registration algorithm proposed by Besl and McKay iteratively aligns two point clouds by optimizing the transformation matrix, ensuring precise matching between models[30]. In recent years, numerous researchers have been devoted to enhancing the classical ICP in order to address issues such as slow convergence[31], low registration efficiency[32-34], and high susceptibility to local optimal solutions[35]. The second aspect focuses on adjusting the position control of the ceramic core, achieved through internal compensation of component positioning within the wax pattern die. Research on workpiece positioning compensation primarily addresses the elimination of positioning errors caused during clamping operations, often by adjusting the length of locator rods to correct workpiece displacement[36, 37]. The above research primarily emphasizes improving the efficiency and accuracy of registration algorithms and methods for workpiece positioning constraints. However, when addressing the positioning limitations of the ceramic core within the wax pattern die, it is essential to consider how variations in the blade's wall thickness tolerance affect the ceramic core's positioning. This consideration is crucial for enhancing the ceramic core-shell registration strategy.

Conventional ICP algorithms typically assume uniform error weights across all points, which may lead to suboptimal registration, particularly in critical regions with thin-walled structures that require more precise alignment. In this study, a blade wall thickness tolerance field was introduced to address this issue. Given the variations in wall thickness tolerances between the leading and trailing edges, as well as the concave and convex regions, and considering the point density differences in these areas, a weight factor for the wall thickness tolerance constraint was defined. This weight ICP approach ensures that regions with tighter tolerances, such as the leading and trailing edges of the blade, are prioritized during the registration and alignment process. Furthermore, a method was proposed to optimize the blade wall thickness deviations by adjusting the position of the ceramic core, with the goal of minimizing excessive variations during the casting process.

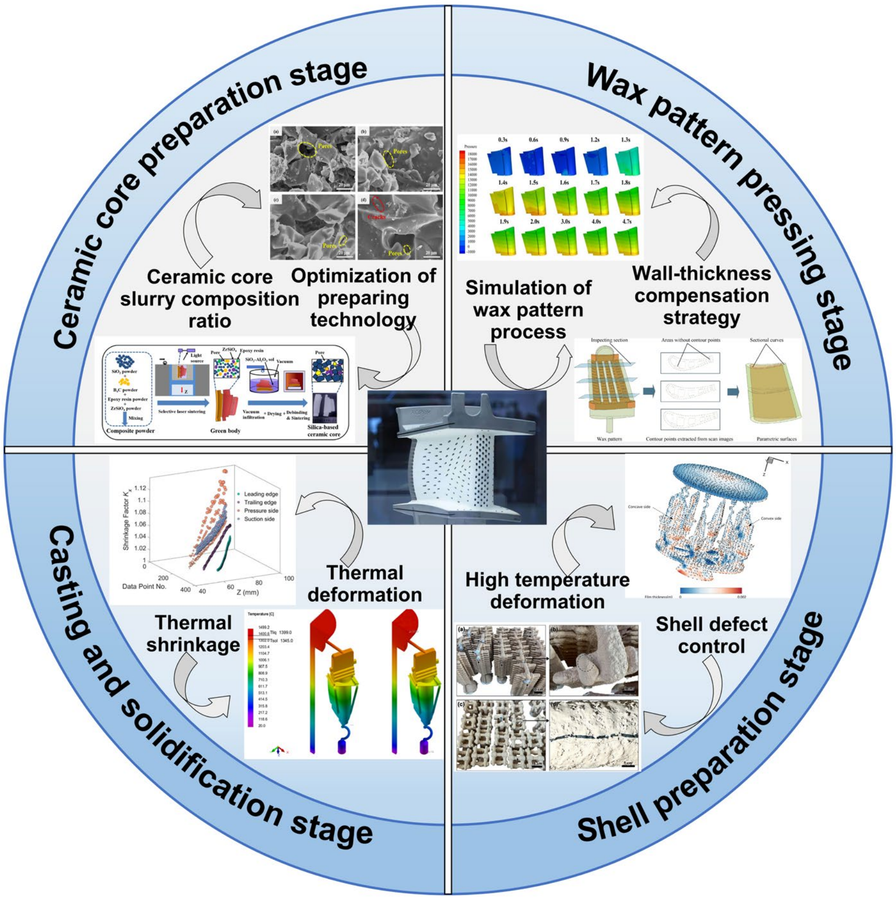

Fig. 1: Main process flow of casting process controls for turbine blade profile/wall thickness

Firstly, internal and external profile data of batch-manufactured blades were collected through industrial computed tomography (ICT). Based on the identified characteristics of wall thickness tolerance deviations, we developed an optimized positioning model for the ceramic core, constrained by the specified tolerance limit. Finally, a reverse adjustment strategy was proposed to modify the initial position of the ceramic core within the wax pattern die.

2 Methodology

As discussed previously, the primary causes of blade wall thickness deviations are identified as positional misalignment of the ceramic core during the investment casting process and surface deformation resulting from thermal softening of the ceramic core, as illustrated in Fig. 2. This study introduced a methodology aimed at mitigating deviations in blade wall thickness caused by positional shifts of ceramic cores during investment casting, as depicted in Fig. 3. The proposed procedure is detailed below:

Step 1: Matching weight definition. The valid data of both internal and external blade profiles are provided by sectional inspection of actual hollow turbine blade castings using ICT. Subsequently, a sectional point cloud sorting algorithm is proposed to indicate the characteristics of the blade's variable wall thickness tolerance.

Step 2: Optimizing ceramic core position. Using the actual internal and external profile data of the blade alongside model matching algorithms, the optimal position of deformed ceramic cores can be determined within the blades.

Step 3: Reversing ceramic core position adjustment. Analyzing the correlation between the actual orientation of the ceramic core and its ideal positioning within the blade, quantifying the deviation of the ceramic core position during casting, and identifying the required adjustment to achieve optimal alignment. Concurrently, correlating this adjustment with the compensation needed for the internal locator rods of the die to ensure precise alignment of the ceramic core, thereby completing the correction of the 'off-center' wax pattern.

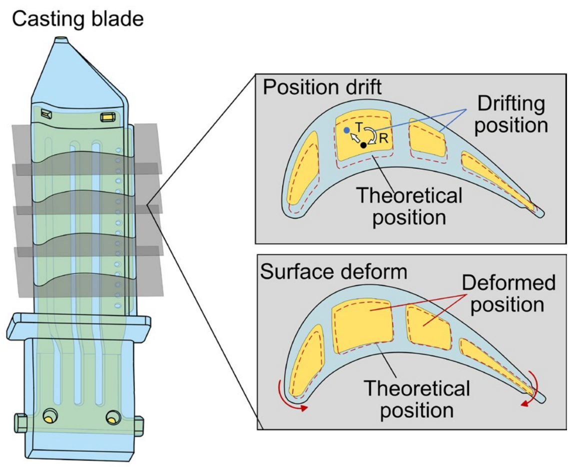

Fig. 2: Analysis of the causes of wall thickness errors

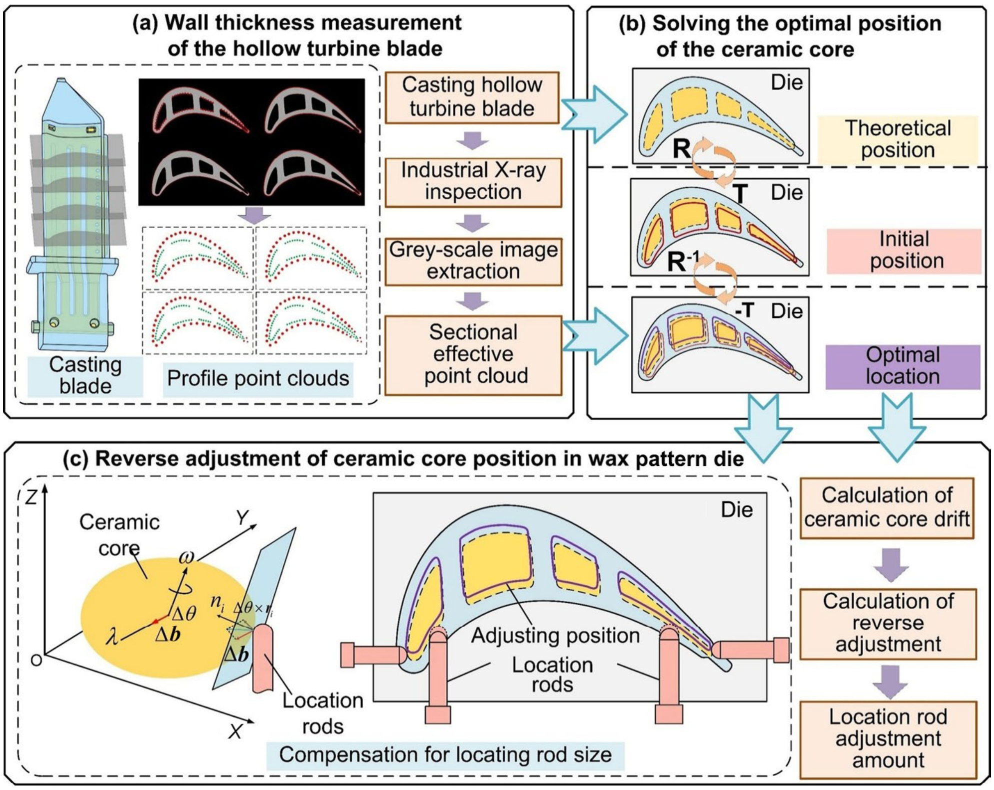

Fig. 3: Method for control of the reverse position of ceramic core: (a) wall thickness measurement of the hollow turbine blade; (b) solving the optimal position of the ceramic core; (c) reverse adjustment of ceramic core position in wax pattern die

2.1 Matching weight definition

2.1.1 Sorting section point cloud

Using ICT technology, five cross-sections at different positions along each blade were chosen to characterize the position of the ceramic core within the blade. To ensure accurate measurement and feature extraction, the level set method was employed for feature extraction based on the discrete point cloud of the cross-section[38, 40]. To segment the point clouds into distinct regions, the point cloud data for the blade sections should be sorted. However, the hollow structure of the blade leads to partial data gaps within the internal blade profile point cloud. These gaps disrupt the proximity characteristics between adjacent points, making it infeasible to directly use the minimum distance between point clouds for sorting. To address this issue, this study constructed a polar coordinate system for each blade section. Utilizing distance-based search techniques, the geometric constraints of the polar coordinate system were introduced to establish an algorithm for sorting the point cloud data of ceramic core sections within the contours of hollow turbine blades, as shown in Fig. 4. The algorithm is described as follows:

Assume that the v-th points on the profile line of the actual ceramic core at the i-th section have already been sorted. The profile point v-th is designated as $\boldsymbol{p}_{iv}$, with its polar angle and radius represented by θ_{iv} and ρ_{iv}, respectively. Therefore, within specified ranges of polar angle, polar radius, and proximity angle, the next point $\boldsymbol{p}_{iv+1}$ along the direction of the ceramic core profile for sorting can be determined. It is defined on the

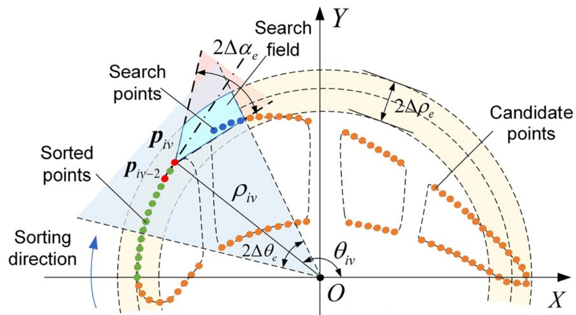

Fig. 4: Algorithm for sorting point clouds in polar coordinates

basis of the Euclidean distance from the current point $\boldsymbol{p}_{iv}$:

$$\begin{aligned} \boldsymbol{p}_{iv+1} &= \min(|\boldsymbol{p}_{ij} - \boldsymbol{p}_{iv}|) \quad (\boldsymbol{p}_{ij} \in \boldsymbol{H}_v) \\ st: & |\theta_{ij} - \theta_{iv}| \le \Delta\theta_e \\ & |\rho_{ij} - \rho_{iv}| \le \Delta\rho_e \\ & \alpha_{ij}^v \le \Delta\alpha_e \end{aligned} \tag{1}$$

$$\alpha_{ij}^v = \arccos((\boldsymbol{p}_{ij} - \boldsymbol{p}_{iv}) \cdot (\boldsymbol{p}_{iv} - \boldsymbol{p}_{iv-2}) / |\boldsymbol{p}_{ij} - \boldsymbol{p}_{iv}| \cdot |\boldsymbol{p}_{iv} - \boldsymbol{p}_{iv-2}|) \tag{2}$$

where $\boldsymbol{H}_v$ represents the set of profile points yet to be sorted; θ_{ij} and ρ_{ij} represent the polar angle value and polar radius value of any remaining search point $\boldsymbol{p}_{ij}$ respectively; $\Delta\boldsymbol{\theta}_e$ and $\Delta\boldsymbol{\rho}_e$ denote the constraints for polar angle and polar radius; α_{ij}^v represents the proximity angle associated with point $\boldsymbol{p}_{ij}$, allowing only points with values below the threshold $\Delta\alpha_e$ to participate in the search. The search range is constrained by the polar angle, polar radius, and proximity angle, ensuring that the closest point to $\boldsymbol{p}_{iv}$ in Euclidean distance is identified as the next closest point to $\boldsymbol{p}_{iv+1}$. This process completes the point cloud sorting for the ceramic core profile.

2.1.2 Division of ceramic core section point cloud

After sorting, the profile points were ordered and interpolated using spline curves. The curvature values of each point were then calculated based on these interpolation spline curves, as shown in Fig. 5. Due to the significant difference in curvature between the leading and trailing edge regions compared to the concave and convex regions of the ceramic core, in the context of geometric shape analysis, a point is deemed to be in the leading and trailing edge region if its curvature value exceeds a critical threshold, denoted as ε_c. This process divides the profile point set $\boldsymbol{H}_L$ and $\boldsymbol{H}_S$ into the leading edge and trailing edge, and concave and convex regions.

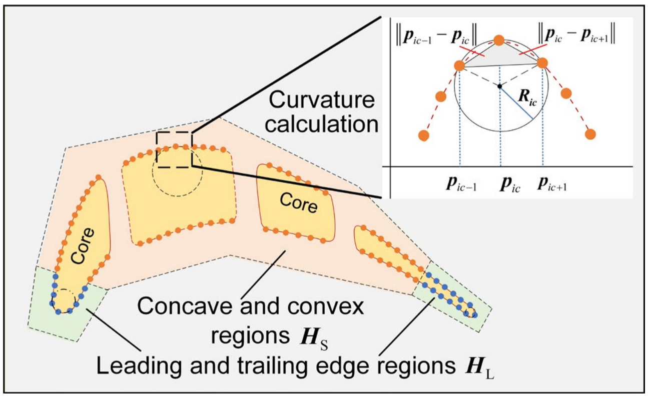

Fig. 5: Method for the division of point cloud regions based on curvature values

Suppose that in the i-th section, the curvature at point $\boldsymbol{p}_{ic}$ is determined using its preceding point $\boldsymbol{p}_{ic\text{-}1}$ and following point $\boldsymbol{p}_{ic+1}$, identified from the sorted point cloud, a curvature circle is constructed from these three points, with the radius $\boldsymbol{R}_{ic}$ derived from the vector length $\|\boldsymbol{p}_{ic\text{-}1}\text{-}\boldsymbol{p}_{ic}\|$ (triangle side length) and the oriented area S_p. Using the section's spline fitting function $B_i(u)$, the curvature radius $\boldsymbol{R}_{ic}$ can be refined. As the neighboring points approach $\boldsymbol{p}_{ic}$ in the limit, the curvature $\boldsymbol{K}_{ic}$ is expressed as the reciprocal of $\boldsymbol{R}_{ic}$, calculated as follows:

$$\boldsymbol{R}_{ic}=\frac{\left\|\boldsymbol{p}_{ic-1}-\boldsymbol{p}_{ic}\right\|\cdot\left\|\boldsymbol{p}_{ic}-\boldsymbol{p}_{ic+1}\right\|\cdot\left\|\boldsymbol{p}_{ic-1}-\boldsymbol{p}_{ic+1}\right\|}{4S} \tag{3}$$

$$S_P=\frac{1}{2}\left|\det((\boldsymbol{p}_{ic-1}-\boldsymbol{p}_{ic})\cdot(\boldsymbol{p}_{ic}-\boldsymbol{p}_{ic+1}))\right| \tag{4}$$

$$\boldsymbol{R}_{ic}=\frac{\sqrt{[B_i(p_{ic-1})-B_i(p_{ic})]^2+1}\cdot\sqrt{[B_i(p_{ic-1})-B_i(p_{ic+1})]^2+4}\cdot\sqrt{[B_i(p_{ic})-B_i(p_{ic+1})]^2+1}}{2\left|B_i(p_{ic-1})-2B_i(p_{ic})+B_i(p_{ic+1})\right|} \tag{5}$$

$$\boldsymbol{R}_{ic}=\lim_{\substack{c-1\to c\\ c+1\to c}}\frac{(1+((B_i'(\boldsymbol{p}_{ic}))^2)^{\frac{3}{2}}}{\left|B_i''(\boldsymbol{p}_{ic})\right|}$$

$$\boldsymbol{K}_{ic}=\frac{1}{R_{ic}} \tag{6}$$

Based on the calculated curvature results of the current sectional point cloud and according to the specified critical curvature threshold ε_c, the sectional point cloud region is divided into leading and trailing edge regions $\boldsymbol{H}_L$ and concave and convex region $\boldsymbol{H}_S$. In this way, the proportional relationship in the weighting factor can be expressed as follows:

$$\begin{aligned}\eta_h&=\frac{S}{M}\\ \eta_l&=\frac{L}{M}\end{aligned}\quad (M=S+L) \tag{7}$$

where η_h is the number of leading and trailing regions proportionality factor; η_l is the number of concave and convex regions proportionality factor; M is the number of point cloud; S is the number of points in concave and convex regions of cloud; and L is the number of points in leading and trailing edge regions of cloud.

2.1.3 Section point cloud weight factor assignment

In general, wall thickness tolerances in the blade area vary. The wall thickness at the leading and trailing edges is thinner and requires stricter tolerance. In contrast, the wall thickness at the concave and convex regions is thicker and has a larger tolerance range. To enhance model matching accuracy for deformed ceramic cores, higher matching weights are assigned to thinner regions with stricter tolerances. Thus, wall thickness, tolerance and point density variations across regions are incorporated into the weight factor calculation, as shown in Fig. 6. The wall thickness tolerance weight factor for a given section is defined as follows:

$$w_{ij}=\begin{cases}\dfrac{(\delta_h+\delta_l)\cdot\boldsymbol{t}_{ij}^{\min}\cdot\eta_i^h}{\delta_h\cdot\boldsymbol{t}_{ij}} & (\boldsymbol{p}_{ij}\in\boldsymbol{H}_L)\\[2ex] \dfrac{(\delta_h+\delta_l)\cdot\boldsymbol{t}_{ij}^{\min}\cdot\eta_j^l}{\delta_l\cdot\boldsymbol{t}_{ij}} & (\boldsymbol{p}_{ij}\in\boldsymbol{H}_S)\end{cases} \tag{8}$$

where $\boldsymbol{H}_L$ and $\boldsymbol{H}_S$ represent sets of contours in the leading and trailing, and the concave and convex of the cores. The $\boldsymbol{t}_{ij}$ is the theoretical value of the wall thickness at the Point $\boldsymbol{p}_{ij}$ on the blade. This value is introduced to ensure that the profile points in the leading and trailing edge regions of the blade have a higher match weight due to their smaller wall thickness values. $\boldsymbol{t}_{ij}^{\min}$ is the minimum theoretical thickness among all points in the i-th section. This value is introduced to eliminate the influence of the size of wall thickness on the weighting factor. The δ_h and δ_l

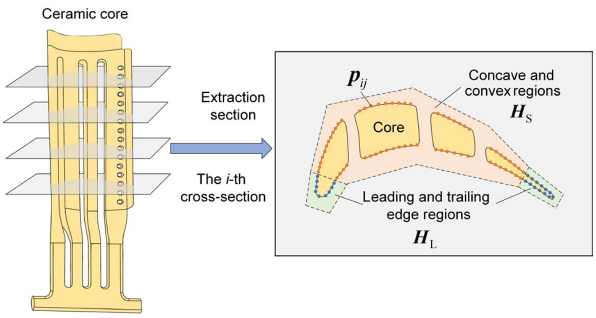

Fig. 6: Wall thickness weight factor tolerance distribution

represents wall thickness tolerances in the leading and trailing edge regions, as well as the concave and convex regions. Introducing this value ensures that profile points in these regions have higher matching weight. To ensure the accuracy of the registration, the quantity compensation coefficients η_i^h and η_i^l are introduced to account for the significant difference of the number of profile points between the leading and trailing edges and the concave and convex regions.

2.2 Optimizing the ceramic core position

By analyzing ICT inspection images, point cloud data of the blade's internal and external contours are extracted. The internal contour shows the profile of the ceramic core, and its position within the blade is determined by the relationship between the internal and external contours. To address contour mismatches, this study introduces an optimal internal profile, constructed using external contour data and design wall thickness specifications. The optimal position of the deformed ceramic core is then determined by aligning the measured internal profile points with this optimized profile.

Figure 7 shows the process for obtaining the optimal thickness profile. The $\boldsymbol{g}_{ij}$ denotes the j-th point on the i-th section of the external profile of the theoretical model of the blade. The optimal position point $\boldsymbol{s}_{ij}$ of the internal profile of the blade thickness can be obtained by inwardly offsetting the points on the external profile of the blade by the thickness value along the normal vector direction.

$$\boldsymbol{s}_{ij}=\boldsymbol{g}_{ij}+\boldsymbol{t}_{ij} \tag{9}$$

where $\boldsymbol{t}_{ij}$ represents the wall thickness direction vector at Point $\boldsymbol{g}_{ij}$ according to the theoretical model. Its value (the theoretical wall thickness) can be expressed as the Euclidean distance between the corresponding point on the outer profile line of the theoretical section of the blade and the tangential point of the inscribed circle tangent to the profile of the theoretical section of the ceramic core. The $F_i^{\text{ins}}(u)$ and $F_i^{\text{out}}(u)$ represent the profile lines inside and outside the theoretical model of the hollow turbine blade, respectively. $\boldsymbol{g}'_{ij}$ is the projection point of Point $\boldsymbol{g}_{ij}$ on $F_i^{\text{out}}(u)$ of the i-th section of the theoretical model of the blade. $\boldsymbol{O}_{ij}^n$ represent a nearby point in the direction of the normal at $\boldsymbol{g}'_{ij}$. The initial position of the center $\boldsymbol{O}_{ij}^n$ of the inscribed circle can be expressed as:

$$\boldsymbol{O}_{ij}^n = \boldsymbol{g}'_{ij} + n \cdot \Delta r \cdot \boldsymbol{n}_g \quad (n=0) \tag{10}$$

where Δr represents the increment of the wall thickness search radius, the n represents the number of iterations for the wall thickness search. The $\boldsymbol{n}_g$ indicates the unit normal vector pointing outward from point $\boldsymbol{g}'_{ij}$ on the blade. Assuming the partial differential values of the parametric section lines of the blade at Point $\boldsymbol{g}'_{ij}$ are $F_{iu}^{\text{out}'}(u_g)$ and $F_{iv}^{\text{out}'}(u_g)$, the unit normal vector $\boldsymbol{n}_g$ can be calculated as follows:

$$\boldsymbol{n}_g = \frac{F_{iu}^{\text{out}'}(u_g) \times F_{iu}^{\text{out}'}(u_g)}{\left| F_{iu}^{\text{out}'}(u_g) \times F_{iu}^{\text{out}'}(u_g) \right|} \tag{11}$$

where u_g represents the parameter value corresponding to a point on the parametric section of the ceramic core. In the theoretical blade model, let $\boldsymbol{s}'_{ij}$ denote the projection of Point $\boldsymbol{g}'_{ij}$ on the section line. The Euclidean distance difference is then calculated among the center $\boldsymbol{O}_{ij}^n$, Point $\boldsymbol{g}'_{ij}$, and its projection $\boldsymbol{s}'_{ij}$.

$$\Delta d_{ij}^n = \left\| \boldsymbol{O}_{ij}^n - \boldsymbol{s}'_{ij} \right| - \left| \boldsymbol{O}_{ij}^n - \boldsymbol{g}'_{ij} \right\| \tag{12}$$

When the distance difference meets the convergence tolerance $\Delta d_{ij}^n \le \varepsilon_0$, the corresponding theoretical wall thickness value of Point $\boldsymbol{g}_{ij}$ can be expressed. Otherwise, let n=n+1, update the position of $\boldsymbol{O}_{ij}^n$ and perform the iterative calculation.

$$\boldsymbol{t}_{ij} = | \boldsymbol{g}'_{ij} - \boldsymbol{s}'_{ij} | \tag{13}$$

The offset point cloud $\boldsymbol{s}'_{ij}$ is subjected to B-spline fitting section curves for the purpose of three-dimensional reconstruction of the optimal wall thickness profile. A wall thickness tolerance weight is introduced to the conventional ICP registration model, based on a wall thickness tolerance constraint:

$$F_2 = \frac{1}{NM} \min \sum_{i=1}^{N} \sum_{j=1}^{M} w_{ij} \left| \boldsymbol{R} \cdot \boldsymbol{p}_{ij} + \boldsymbol{T} - \boldsymbol{p}_{ij}^b \right|^2 \tag{14}$$

where $\boldsymbol{p}_{ij}^b$ is the projection point on the optimal wall thickness profile; $\boldsymbol{p}_{ij}$ represents the j-th profile point of the i-th section at the initial position of the ceramic core, while $\boldsymbol{q}_{ij}$ denotes

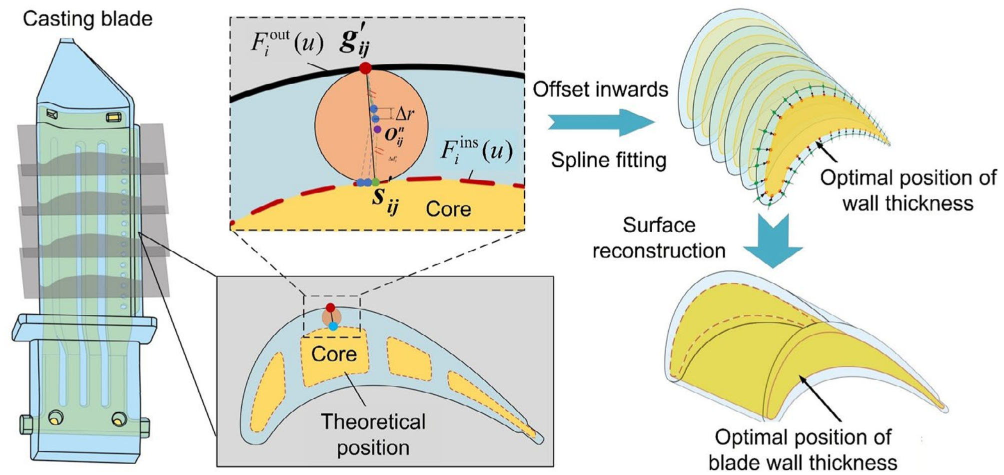

Fig. 7: Construction of optimal wall thickness profile

the projection point of $\boldsymbol{p}_{ij}$ on the actual blade optimal wall thickness. w_{ij} is the weighting factor corresponding to Point $\boldsymbol{p}_{ij}$. N represents the number of sections of the ceramic core, and M represents the number of points in each section. The optimal position base model of the ceramic core is solved using the SVD algorithm to obtain the optimal adjustment parameters. The angle parameters for rotation along the X, Y, Z axes are denoted as: $\Delta\boldsymbol{\varphi}_x$, $\Delta\boldsymbol{\varphi}_y$, $\Delta\boldsymbol{\varphi}_z$, while the translation parameters for movement along the X, Y, Z axes are denoted as: $\Delta\boldsymbol{\delta}_x$, $\Delta\boldsymbol{\delta}_y$, $\Delta\boldsymbol{\delta}_z$. The optimal position of any point $\boldsymbol{p}_{ij}$ on the ceramic core within the blade is represented as:

$$\boldsymbol{p}'_{ij} = \Delta\boldsymbol{R}\cdot\boldsymbol{p}_{ij} + \Delta\boldsymbol{T} \tag{15}$$

The parameters are as follows:

$\Delta\boldsymbol{R}=[\Delta\boldsymbol{\varphi}_x\Delta\boldsymbol{\varphi}_y\Delta\boldsymbol{\varphi}_z]^{\mathrm{T}}$ – rotation vector;

$\Delta\boldsymbol{T}=[\Delta\boldsymbol{\delta}_x\Delta\boldsymbol{\delta}_y\Delta\boldsymbol{\delta}_z]^{\mathrm{T}}$ – translation vector;

$\boldsymbol{p}_{ij}$ – the point of the initial position of the ceramic core;

$\boldsymbol{p}'_{ij}$ – the point of the optimal position of the ceramic core.

2.3 Reversing ceramic core position adjustment

To mitigate the impact of ceramic core positional shift on blade wall thickness deviation, it is necessary to adjust the initial position of the ceramic cores within the wax mold in a reverse manner. Consequently, a method was proposed for inversely adjusting the ceramic core positions by compensating for the wax pattern die location. The adjustment amount is determined inversely based on the calculated ceramic core position shift, establishing a mapping relationship between this adjustment and the compensation of the internal locator rod size in the die. This approach ultimately alters the initial position of the ceramic core.

Figure 8 shows the positional relationship of the core before and after the reverse adjustment. The position of the core within the wax pattern die, particularly its initial placement within the shell, is determined by the principle of reverse deformation. If the surface equation of the actual core before registration is denoted by $\boldsymbol{S}_{\mathrm{D}}(u, v)$, the surface equation of the core after reverse adjustment within the mold, based on the rotation matrix $\boldsymbol{R}'$ and the translation vector $\boldsymbol{T}'$ obtained from the registration model, can be expressed as:

$$\boldsymbol{S}_{\mathrm{D}}(u,v) = \sum_{e=0}^{N}\sum_{f=0}^{E}(\boldsymbol{R}'\boldsymbol{h}_{ef}^{\mathrm{D}} + \boldsymbol{T}')B_{e,k}(u)B_{f,k}(v) \tag{16}$$

where $\boldsymbol{h}_{ef}^{\mathrm{D}}$ represents the control vertices of the reconstructed actual core surface before registration. The e and f represent the number of splines and sections. The reconstructed position of the actual core surface reflects its initial placement within the wax pattern die.

The position of the ceramic core within the blade is primarily determined by its position within the wax pattern die of the blade, facilitated by internal locator rods within the die. To adjust the initial position of the ceramic core within the shell, compensation must be made for the dimensions of the internal ceramic core locator rods within the wax pattern die. The adjustment mechanism assumes the ceramic core undergoes rigid-body displacement within the wax pattern die. Due to the high stiffness of the ceramic core and moderate wax injection pressure, elastic deformation of the core and die is negligible in this stage.

In general, the location rod inside the die and the contact end of the ceramic core surface is hemispherical in shape, as shown in Fig. 9. The $\boldsymbol{G}_0$ represents the initial position of the center of the contact sphere of the location rod, the $\boldsymbol{\tau}$ denotes the unit normal vector along the length direction of the location rod, and the r represents the radius of the contact sphere of the locator rod. Therefore, the compensation required for the locator rod dimensions can be calculated using the following method:

Step 1: According to the calculation results of the position reversal adjustment, the three-dimensional surface of the ceramic core is moved to the target position.

Step 2: Calculate the distance D_0 between the sphere center and the transformed surface of the ceramic core, and then determine the searching direction. If $D_0 - r \geq 0$, set the searching direction: $\boldsymbol{\tau}$; otherwise, set the searching direction: $-\boldsymbol{\tau}$.

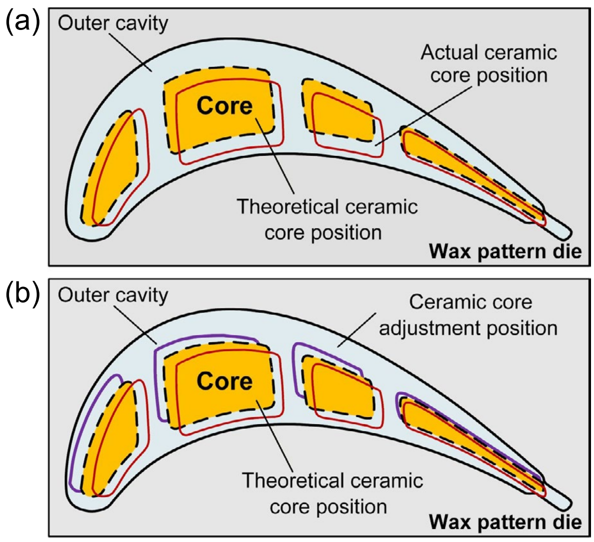

Fig. 8: Change in the position of ceramic core within the die cavity before (a) and after (b) adjustment

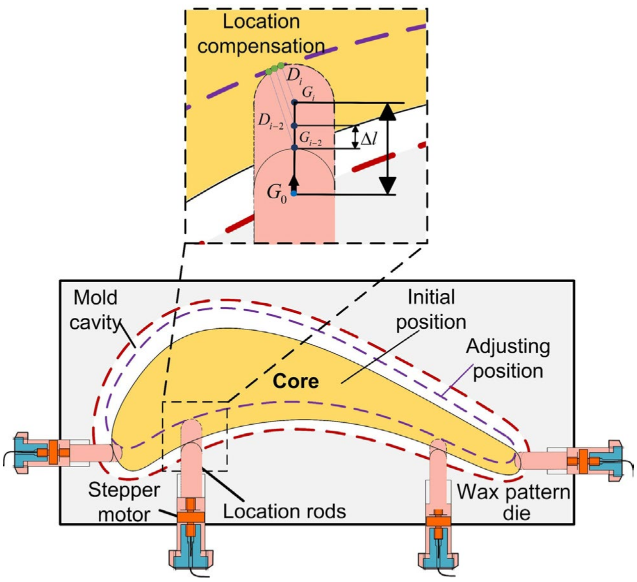

Fig. 9: Calculating dimensional compensation of location rods

Step 3: Set a searching increment Δl; when $|D_n-r|\geq\eta$ (η represents the convergence tolerance), the center position of the contact ball of the location rod must be updated:

$$\boldsymbol{G}_n=\boldsymbol{G}_0\pm\boldsymbol{n}\cdot\Delta l\cdot\boldsymbol{\tau} \quad (17)$$

Step 4: Calculate the distance ΔS between the center of the location rod contact ball and the surface of the ceramic core. When $|D_n-r|<\eta$, it is assumed that the contact surface of the location rod and the surface of the ceramic core are in contact, and the iteration is stopped. At this point, the location rod size compensation amount is $\boldsymbol{\Delta S}=\boldsymbol{n}\cdot\boldsymbol{\Delta l}$ and the positioning compensation location is $\boldsymbol{\tau}$.

3 Experiment and analysis

To evaluate the positional shift characteristics of ceramic cores, a total of twelve turbine blades from two different production modules were selected as representative inspection samples. The profile point cloud data of the actual blade sections were obtained in the sequence of leading edge, trailing edge, concave and convex, as show in Fig. 10.

3.1 Solving optimal position of ceramic core

Based on the measured data of the inner and outer contours of the blades, the optimal position of the actual ceramic core inside the blade was determined. The point cloud of the cross-section was first divided into regions, and then the inner profile points of the blade were sorted and divided. The relevant point cloud sorting and curvature threshold parameters are presented in Table 1. The curvature values of each point in the ordered point cloud are displayed in Fig. 11. It is evident that two distinct positions with abrupt curvature change. Specifically, the curvature values of the point cloud increase in the regions corresponding to the leading and trailing edges, where larger curvatures are observed.

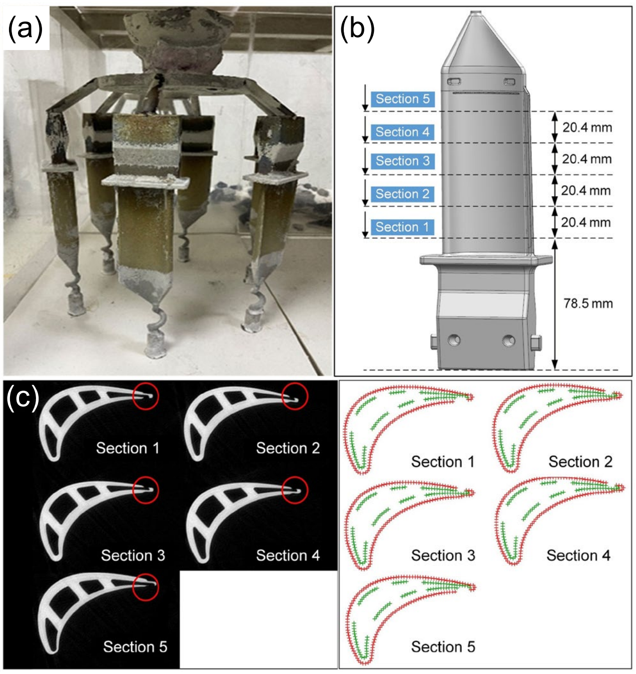

Fig. 10: Two batches of blade castings: (a) batch-produced casting blades; (b) position of cross-section detection; (c) partial cross-section grayscale image and profile points

Based on the regional segmentation results, weight factors were assigned. Using a specific cross-section of a ceramic core as an example, weight factors were allocated across the cross-section, followed by overall three-dimensional registration. The weight factors at each point for the five cross-sections are illustrated in Fig. 12. It can be observed that larger weight factors are assigned to the leading and trailing edge regions, while smaller weight factors are assigned to the concave and convex regions.

Table 1: Sorting parameters for the ceramic core cross-section point cloud

Polar radius error (mm)	Polar angle error (rad)	Proximity angle value (mm)	Curvature threshold (mm)
0.3	0.05	0.025	0.3

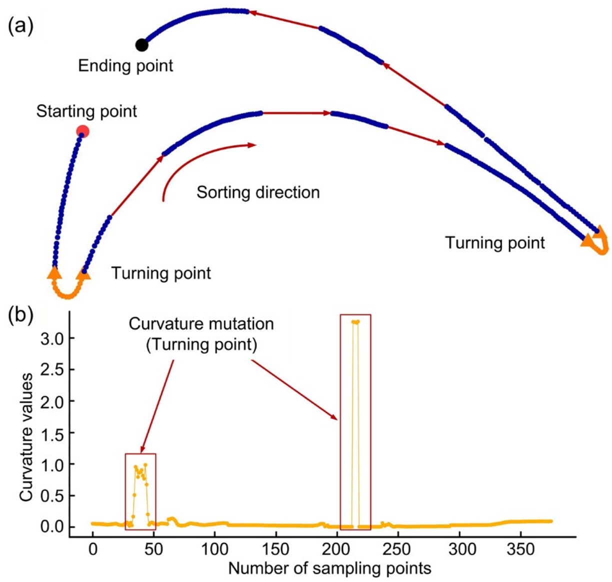

Fig. 11: Cross-section point cloud region segmentation based on curvature difference: (a) sorting result of point cloud of ceramic core cross-section; (b) curvature variation of the ordered point cloud in the cross-section

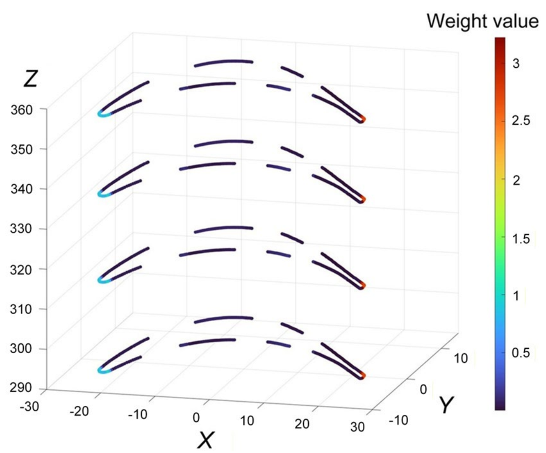

Fig. 12: Cross-section points cloud weight allocation

On this basis, a three-dimensional rigid registration calculation was performed between the actual ceramic core point cloud and the optimal blade wall thickness. A comparative analysis was conducted with the traditional ICP algorithm, and the results are presented in Table 2. After registration, the maximum error between the actual ceramic core and the optimal blade wall thickness is approximately 0.0772 mm. The section point cloud is matched with the model after weight distribution to find the optimal position of the ceramic core. Ten measurement points each from the leading edge, trailing edge, concave surface, and convex surface were selected to compare the wall thickness before and after profile registration against theoretical values, as illustrated in Fig. 13(a). Through the detection and analysis of the actual blade wall thickness, as shown in Fig. 13(b), red points represent the theoretical wall thickness, black points indicate the initial position, and blue points are the optimal position. The results indicate that, after registration with the weight factor, the optimal spatial position of the ceramic core approaches the theoretical wall thickness more closely: approximately 1.2 mm at the leading edge (reduced from about 1.6 mm) and 0.2 mm at the trailing edge (reduced from about 0.5 mm). Additionally, the concave and convex areas also align significantly closer to the theoretical wall thickness values. The optimal core position aligns closer to the theoretical wall

Table 2: Comparison of weighted ICP and traditional ICP algorithm

Parameters	Traditional ICP	Weighted ICP
$\Delta\alpha$°	0.1354	0.1404
$\Delta\beta$°	0.0222	0.0169
$\Delta\gamma$°	−0.2649	−0.2263
Δx (mm)	0.2642	0.2593
Δy (mm)	0.1694	0.1408
Δz (mm)	−0.0414	−0.0358
Maximum error (mm)	0.1193	0.0772
Iteration	50	50

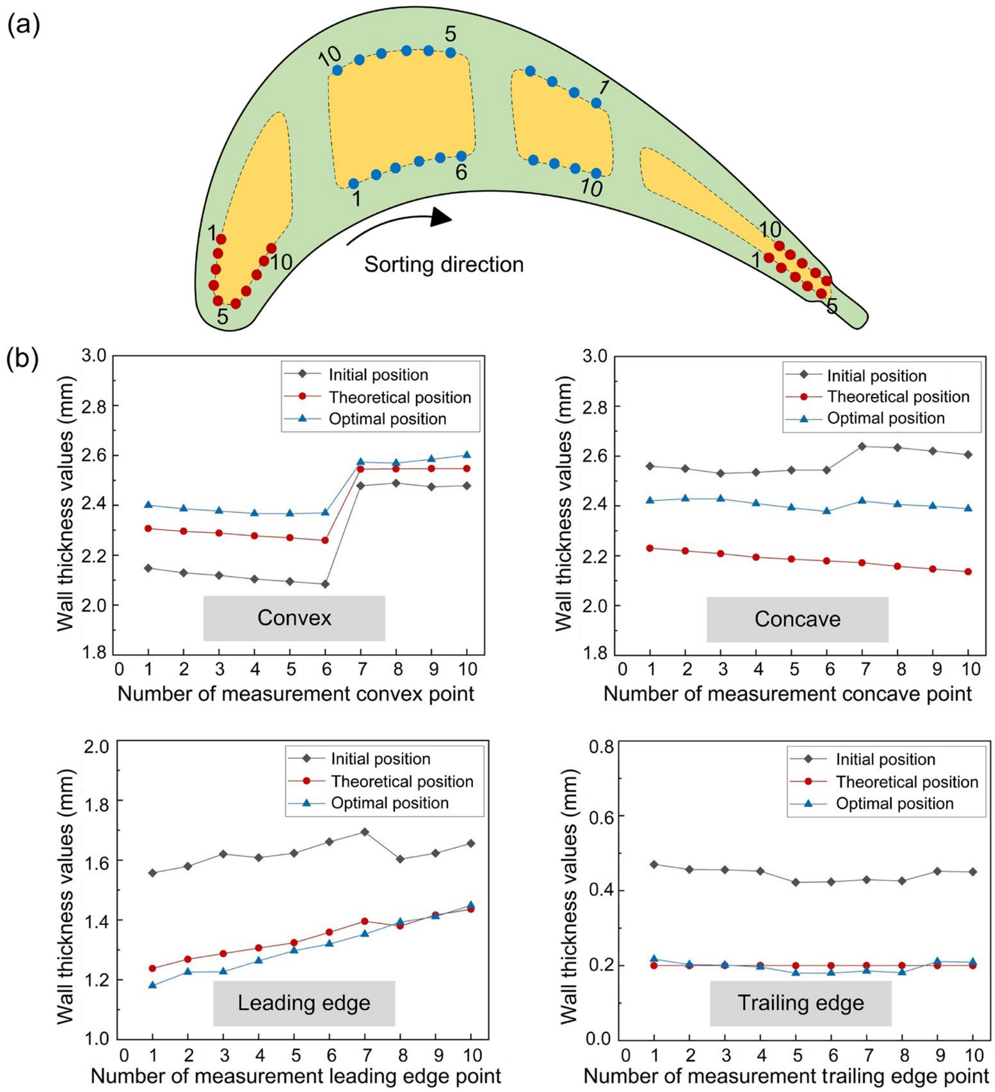

Fig. 13: Comparative analysis of the wall thickness (cross-section): (a) cross-section position sampling; (b) wall thickness measurement results

thickness. This emphasizes the viability of the algorithm. Next, the shift amounts of the ceramic core positions for the six blades are determined based on the relationship between the core positions. Consistency in the shift trends of the ceramic cores across the batch-produced blades is noted, further confirming the average shifting value, as shown in Table 3.

After acquiring the results of the actual batch production blade shift, the target orientation adjusted by the ceramic core within the wax mold space was inversely solved. Consequently, the dimensional compensation of the location rods in the wax pattern die was calculated. In this experiment, six sets of ceramic cores, which conform to the allowable mold manufacturing errors, were selected for wax injection pressing and casting trials. Figure 14 illustrates the distribution of location rods inside the wax pattern die, while Table 4 presents the calculated dimensional compensation values for these rods.

Table 3: Ceramic core positional shifting values

Sample No.	ΔT_x	ΔT_y	ΔT_z	$\Delta\alpha$	$\Delta\beta$	$\Delta\gamma$
1	0.2795	–0.1698	0.0337	0.1887	–0.2032	0.0457
2	0.2567	–0.1449	0.0378	0.1588	–0.2558	0.0447
3	0.3226	–0.1428	0.0397	0.1525	–0.2537	0.0473
4	0.2424	–0.1460	0.0388	0.1607	–0.2238	0.0415
5	0.2478	–0.1430	0.0392	0.1659	–0.2588	0.0476
6	0.3013	–0.1253	0.0315	0.1579	–0.2496	0.0541
7	0.2585	–0.1099	0.0298	0.1366	–0.2051	0.0517
8	0.2842	–0.1514	0.0199	0.1472	–0.2254	0.0426
9	0.2549	–0.1124	0.0248	0.1455	–0.2063	0.0522
10	0.2674	–0.1149	0.0186	0.1544	–0.2112	0.0507
11	0.2916	–0.1495	0.0098	0.1762	–0.2271	0.0391
12	0.3162	–0.1258	0.0137	0.1825	–0.2137	0.0536
Average	0.2769	–0.1363	0.0281	0.1606	–0.2278	0.0476

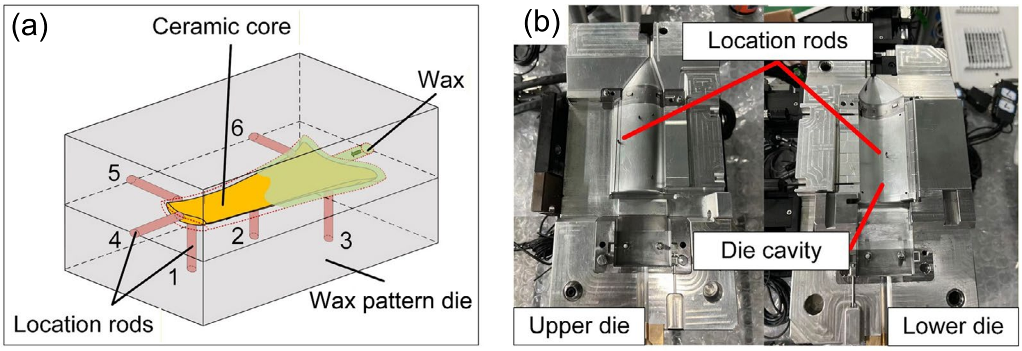

Fig. 14: Distribution of locator rods within the wax pattern die (a), calibration of the physical positions of the mold's locating rods (b)

Table 4: Movement size of the location rods of the wax pattern die

Locator rod	No. 1	No. 2	No. 3	No. 4	No. 5	No. 6
Value (mm)	0.56	0.53	–0.52	1.23	0.52	–0.49

3.2 Wax pressing and wall thickness analysis

Figures 15(a) and (b) show the wax injection equipment and the resulting "off-center" wax pattern, with the process parameters summarized in Table 5. To validate the alignment of the ceramic core with the locator rods, the wall thickness of the wax pattern is measured ultrasonically. The sampling points for wall thickness measurements are shown in Fig. 16(a), while the measured values are compared to the theoretical wall thickness in Fig. 16(b). Results indicate that the average wall thickness for the convex and concave surfaces is 2.4 mm and 2.0 mm, respectively, confirming the effectiveness of the positioning adjustments.

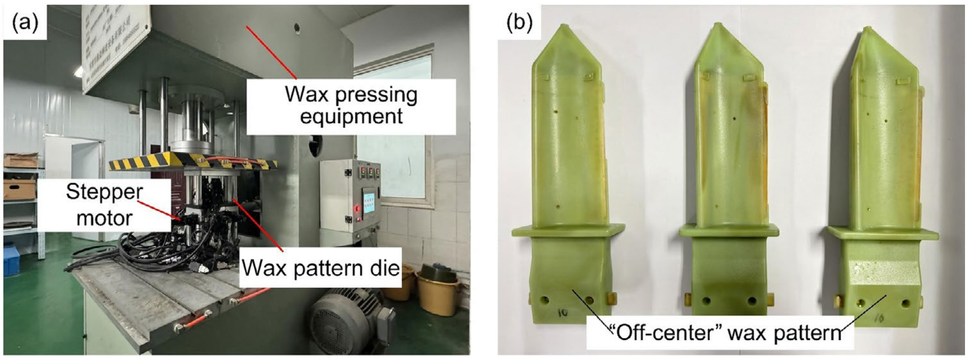

Fig. 15: Waxing equipment (a) and "off center" wax patterns (b)

Table 5: Wax pressing process parameters

Injection pressure (MPa)	Holding pressure (MPa)	Wax temperature (°C)	Mold temperature (°C)	Pressure holding time (s)	Cooling time (s)
1.0	1.0	75	20	20	20

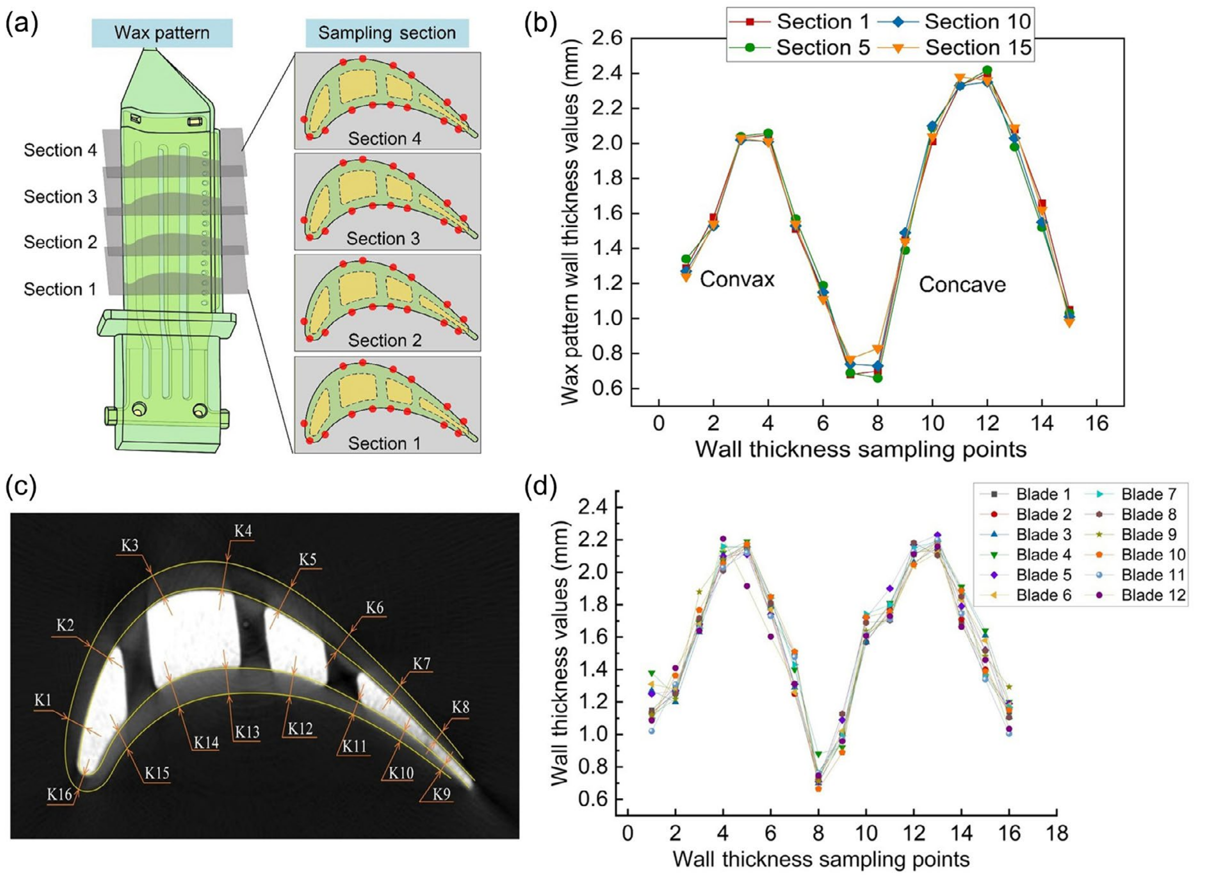

Fig. 16: Wax pattern wall thickness sampling points (a), wax pattern wall thickness values (b), ICT of sampling points in wax pattern section (c), and wall thickness values (d)

3.3 Precision casting experimental validation and analysis

To verify whether adjusting the positions of ceramic cores can maintain the wall thickness deviation of the blades within the tolerance range, eight blades, as shown in Fig. 17, were selected from the actual casting results. The blades were inspected using ICT scanning to obtain accurate internal and external profile data. The ceramic core shift was recalculated. Compared with pre-adjustment data, the average shifting of the ceramic core along the X, Y, and Z axes during casting is reduced, as detailed in Fig. 18.

Using an ICT measuring instrument, four cross-sections of each blade were sampled to measure the wall thickness. To accurately quantify the reduction in wall thickness error, the average wall thickness error was defined as the mean absolute deviation between the measured and theoretical values across

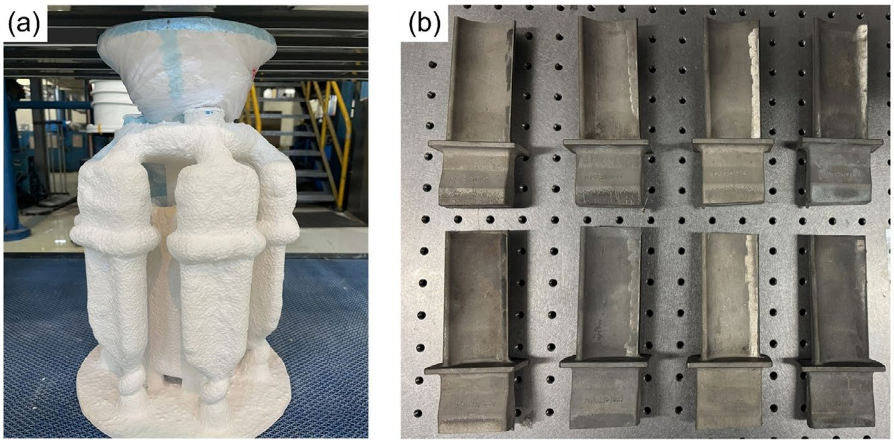

Fig. 17: Casting experiment verification: (a) shell; (b) casting blades

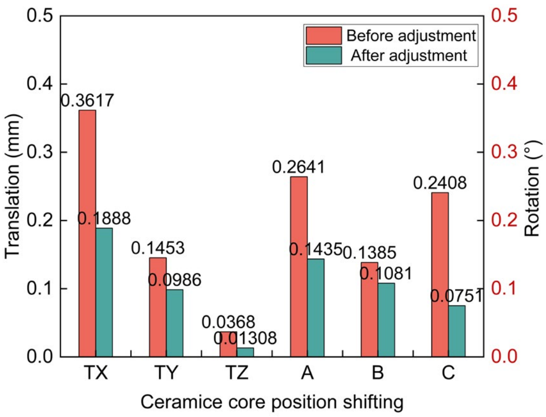

Fig. 18: Comparison of the positional shift of the adjusted ceramic core of the blade

all sampled points:

$$\overline{E}=\frac{1}{N}\sum_{j=1}^{N}\left|t_j^{\text{meas}}-t_j^{\text{theor}}\right| \tag{18}$$

where t_j^{meas} and t_j^{theor} are the measured and theoretical wall thickness at the j-th point, and N is the total number of points across selected cross-sections. The percentage reduction is defined as:

$$\Delta E\%=\frac{\overline{E}_{\text{before}}-\overline{E}_{\text{after}}}{\overline{E}_{\text{before}}}\times 100\% \tag{19}$$

According to the above equation, the average wall thickness error for the critical section was calculated from eight blades, as shown in Fig. 19. After adjusting the ceramic core positions using this method, the average wall thickness error (absolute

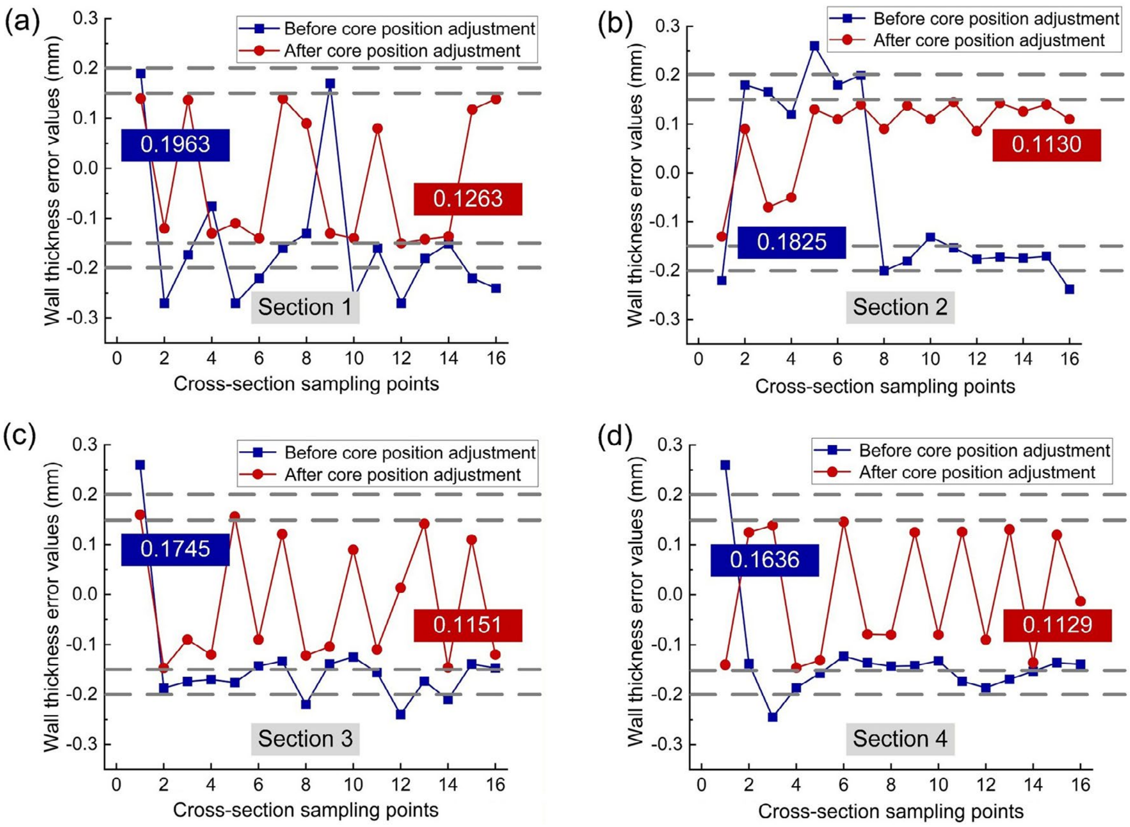

Fig. 19: Comparison of wall thickness errors in blade sections: (a) Section 1; (b) Section 2; (c) Section 3; (d) Section 4

value) in Section 1 decreases from 0.1963 to 0.1263, that in Section 2 decreases from 0.1825 to 0.1130, that in Section 3 decreases from 0.1745 to 0.1151, and that in Section 4 decreases from 0.1636 to 0.1129. It is calculated that the average errors of the four cross-sections have decreased by 33.66%, 38.08%, 45.50%, and 30.99% respectively compared with those before adjustment. The wall thickness error essentially meets the requirements for blade wall thickness deviation (leading and trailing edges: ±0.15 mm, concave and convex: ±0.2 mm), resulting in blades with more uniform wall thickness.

4 Conclusions and outlook

This study presented a method to reduce wall thickness deviations in hollow turbine blades caused by ceramic core displacement during casting. The main findings are as follows:

(1) A reverse positioning framework is established based on ICT-measured internal profiles and a tolerance-weighted registration model, enabling accurate determination of the optimal ceramic core position.

(2) A geometric mapping scheme is proposed to translate core shift into locator rod compensation in the wax pattern die, allowing precise pre-casting correction of the ceramic core orientation.

(3) Casting experiments validate the effectiveness of the tolerance-constrained inverse adjustment method. The results illustrate that after adjustment, the maximum wall thickness error of the blade is reduced by 45.5% compared to the initial one. Errors in critical regions are reduced to within ±0.15 mm (leading/trailing edges) and ±0.2 mm (concave/convex surfaces), meeting the requirement for tolerances.

Although the proposed method effectively improves the wall thickness precision of hollow turbine blades, challenges remain. Reverse deviations in the ceramic core position can alter the casting flow field, potentially varying the pressure exerted by the molten metal on the ceramic core surface, causing subtle positional shifts. Ensuring complete alignment between the ceramic core and the optimal blade wall thickness position remains challenging. Future research may involve iterative displacement analysis to further enhance the control of wall thickness in hollow turbine blades.

Acknowledgments

The authors would like to express their gratitude for the financial support of the National Natural Science Foundation of China (Grant No. 52005311) and the Research Project Supported by Shanxi Scholarship Council of China (Grant No. 2023-003).

Conflict of interest

The authors declare that they have no known competing financial interests or personal relationships that could have appeared to influence the work reported in this paper.

References

[1] Town J, Straub D, Black J, et al. State-of-the-art cooling technology for a turbine rotor blade. Journal of Turbomachinery, 2018, 140(7): 071007.

[2] Chowdhury T S, Mohsin F T, Tonni M M, et al. A critical review on gas turbine cooling performance and failure analysis of turbine blades. International Journal of Thermofluids, 2023, 18: 100329.

[3] Wang W, Yan Y, Zhou Y, et al. Review of advanced effusive cooling for gas turbine blades. Energies, 2022, 15: 8568.

[4] Huang Y, Wei M, Xiao G, et al. Allowance extraction considering of inner and outer contour and experimental research on belt grinding of hollow blade. Chinese Journal of Mechanical Engineering, 2023, 36: 69.

[5] Liang X, Zhao Y, Ma D, et al. Study on the preparation and microstructure of a single-crystal hollow turbine blade. Materials and Manufacturing Processes, 2017, 32: 1887–1892.

[6] Zhou L, Wang D, Cui J, et al. Modeling and experimental study on deformation prediction of thin-walled turbine blades during investment casting process. Proceedings of the Institution of Mechanical Engineers, Part B: Journal of Engineering Manufacture, 2024, 238(1–2): 223–234.

[7] Liu C, Jin S, Lai X, et al. Influence of complex structure on the shrinkage of part in investment casting process. The International Journal of Advanced Manufacturing Technology, 2015, 77: 1191–1203.

[8] Chen S, Sun D, Wang C, et al. Alumina-based ceramic mold with integral core and shell for hollow turbine blades fabricated by laser powder bed fusion. Additive Manufacturing, 2022, 58: 103046.

[9] Zhao D, Zhou L, Wang D, et al. Integrated computational framework for controlling dimensional accuracy of thin-walled turbine blades during investment casting. The International Journal of Advanced Manufacturing Technology, 2023, 129: 1315–1328.

[10] Li H, Hu K, Liu Y, et al. Improved mechanical properties of silica ceramic cores prepared by 3D printing and sintering processes. Scripta Materialia, 2021, 194: 113665.

[11] Pan Z, Guo J, Li S, et al. Experimental study on high temperature performances of silica-based ceramic core for single crystal turbine blades. Ceramics International, 2022, 48(1): 548–555.

[12] Xuan W, Zhang Q, Song H, et al. Improved mechanical properties and dimensional accuracy of silica-based ceramic cores by Si_3N_4 addition. Ceramics International, 2024, 50(14): 25730–25737.

[13] Bazhenov V E, Sannikov A V, Kovyshkina E P, et al. The influence of injection temperature and pressure on pattern wax fluidity. Journal of Manufacturing and Materials Processing, 2023, 7(4): 141.

[14] Barati E, Akbari J. The effect of injection parameters on dimensional accuracy of wax patterns for investment casting. Journal of Computational and Applied Research in Mechanical Engineering, 2020, 9: 313–322.

[15] Pattnaik S, Karunakar D B, Jha P K. Influence of injection process parameters on dimensional stability of wax patterns made by the lost wax process using Taguchi approach. Proceedings of the Institution of Mechanical Engineers, Part L: Journal of Materials Design and Applications, 2013, 227: 52–60.

[16] Wang D, He B, Li F, et al. Cavity pressure and dimensional accuracy analysis of wax patterns for investment casting. Materials and Manufacturing Processes, 2013, 28: 637–642.

[17] Bonilla W, Masood S H, Iovenitti P. An investigation of wax patterns for accuracy improvement in investment cast parts. The International Journal of Advanced Manufacturing Technology, 2001, 18(5): 348–356.
[18] Wang D, He B, Li F, et al. Numerical simulation of the wax injection process for investment casting. Materials and Manufacturing Processes, 2013, 28: 220–224.
[19] Wang D, He B, Liu S, et al. Dimensional shrinkage prediction based on displacement field in investment casting. The International Journal of Advanced Manufacturing Technology, 2016, 85: 201–208.
[20] Wang N, Wang W, Jiang R, et al. Ceramic core shifting monitoring through clamping rods optimization for wax pattern of turbine blade. The International Journal of Advanced Manufacturing Technology, 2017, 91: 2193–2204.
[21] Cui K, Jing L, Jiang R, et al. Core shift limitation in investment casting process of hollow turbine blade. Chinese Journal of Aeronautics, 2023: 1–14.
[22] Cui K, Wang W, Jiang R, et al. A wall-thickness compensation strategy for wax pattern of hollow turbine blade. Chinese Journal of Aeronautics, 2019, 32: 1982–1993.
[23] Jiang R, Zhang D, Bu K, et al. A deformation compensation method for wax pattern die of turbine blade. The International Journal of Advanced Manufacturing Technology, 2017, 88: 3195–3203.
[24] Dong R, Wang W, Cui K, et al. An investigation of ceramic shell thickness uniformity and its impact on precision in turbine blade investment casting. Journal of Manufacturing Processes, 2024, 131: 507–522.
[25] Zhao D, Wang D, Zhou L, et al. Effect of mold dwell time on shrinkage defects in investment casting of superalloy turbine blade. The International Journal of Advanced Manufacturing Technology, 2024, 132: 4473–4487.
[26] Wang Z H, Wang J, Yu L B, et al. Numerical simulation and process optimization of vacuum investment casting for Be-Al alloys. International Journal of Metalcasting, 2019, 13: 74–81.
[27] Dong Y W, Bu K, Dou Y Q, et al. Determination of wax pattern die profile for investment casting of turbine blades. Transactions of Nonferrous Metals Society of China, 2011, 21(2): 378–387.
[28] Ren S, Bu K, Mou S, et al. Control of dimensional accuracy of hollow turbine blades during investment casting. Journal of Manufacturing Processes, 2023, 99: 548–562.
[29] Ren S, Bu K, Zhang R, et al. Effect of constraint removal on single-crystal blade dimensions during investment casting. Journal of Manufacturing Processes, 2024, 119: 73–86.
[30] Besl P J, Mckay N D. A method for registration of 3-D shapes. In: Proceedings of SPIE – The International Society for Optical Engineering, 1992, 14(3): 239–256.
[31] Li J, Hu Q, Zhang Y, et al. Robust symmetric iterative closest point. ISPRS Journal of Photogrammetry and Remote Sensing, 2022, 185: 219–231.
[32] Yang X, Liu X L, Liu J M, et al. Matching algorithm for profile error calculation of blade surface. Advanced Materials Research, 2016, 1136: 630–635.
[33] Cao L, Zhuang S, Tian S, et al. A global structure and adaptive weight aware ICP algorithm for image registration. Remote Sensing, 2023, 15(12): 3185.
[34] Naus K, Marchel Ł. Use of a weighted ICP algorithm to precisely determine USV movement parameters. Applied Sciences, 2019, 9(17): 3530.
[35] Wang Y, Solomon J. Deep closest point: Learning representations for point cloud registration. In: Proc. 2019 IEEE/CVF International Conference on Computer Vision (ICCV), Seoul, the Republic of Korea, 2019, 3522–3531.
[36] Li B, Tian W, Zhang C, et al. Positioning error compensation of an industrial robot using neural networks and experimental study. Chinese Journal of Aeronautics, 2022, 35: 346–360.
[37] Zhu S W, Ding G F, Ma S W, et al. Workpiece locating error prediction and compensation in fixtures. The International Journal of Advanced Manufacturing Technology, 2013, 67: 1423–1432.
[38] Dong R Z, Wang W H, Cui K, et al. Core shifting prediction in filling process of hollow turbine blade investment casting. Journal of Manufacturing Processes, 2023, 86: 253–265.
[39] Li Z, Tang S, Sun T, et al. A convex level-set method with multiplicative-additive model for image segmentation. Applied Mathematical Modelling, 2024, 132: 587–606.
[40] Huang K, Li Z, Tang S, et al. A level-set method with the 3D multiplicative-additive model for CT volume data segmentation. Measurement, 2024, 229: 114442.